Monthly Notices
of the
ROYAL ASTRONOMICAL SOCIETY

MNRAS **463,** 520–528 (2016) doi:10.1093/mnras/stw1910

The stability of the crust of the dwarf planet Ceres

M. Formisano,* C. Federico,* S. De Angelis,* M. C. De Sanctis and G. Magni
INAF–IAPS, Via del Fosso del Cavaliere 100, 00133 Roma, Italy

Accepted 2016 July 28. Received 2016 July 28; in original form 2016 April 12

ABSTRACT

In this article, we study the possibility that Ceres has, or had in the past, a crust heavier than a pure or muddy ice mantle, in principle gravitationally unstable. Such a structure is not unusual in the Solar system: Callisto is an example. In this work, we test how the composition (i.e. the volumetric quantity of ice) and the size of the crust can affect its survival during thermophysical evolution after differentiation. We have considered two different configurations: the first characterized by a dehydrated silicate core and a mantle made of pure ice, the second with a hydrated silicate core and a muddy mantle (ice with silicate impurities). In both cases, the crust is composed of a mixture of ice and silicates. These structures are constrained by a recent measurement of the mean density by Park et al. The Rayleigh–Taylor instability, which operates in such an unstable structure, could reverse all or part of the crust. The whole unstable crust (or part of it) can interact chemically with the underlying mantle and what is currently observed could be a partially/totally new crust. Our results suggest that, in the case of a pure ice mantle, the primordial crust has not survived until today, with a stability timespan always less than 3 Gyr. Conversely, in the case of a muddy mantle, with some 'favourable' conditions (low volumetric ice percentage in the crust and small crustal thickness), the primordial crust could be characterized by a stability timespan compatible with the lifetime of the Solar system.

Key words: minor planets, asteroids: individual: Ceres – planets and satellites: interiors.

1 INTRODUCTION

The dwarf planet (1) Ceres, the second target of the National Aeronautics and Space Administration (NASA) *Dawn* mission after (4) Vesta (Russell & Raymond 2011), is the largest object in the asteroid main belt. Unlike asteroid (4) Vesta, the surface of which is characterized substantially by igneous materials (De Sanctis et al. 2012) and for which we have representative samples (howardite–eucrite–diogenite (HED) meteorites: McSween et al. 2013), the observed surface of Ceres lacks similar igneous rocks (De Sanctis et al. 2015). This difference in the observations led to the conclusion that Vesta likely has a differentiated interior, while the case of Ceres does not suggest an internal differentiated structure. Moreover, there are no meteorites on the Earth supposed to have originated directly from Ceres, although its surface composition is partly consistent with carbonaceous chondrites (Rivkin, Asphaug & Bottke 2014). Thus, we do not have any direct sample to test the differentiation hypothesis in the laboratory. The lack of a collisional family is probably due to the sublimation of possible fragments coming from the ice mantle after ejection (Milani et al. 2014; Rivkin et al. 2014).

* E-mail: michelangelo.formisano@iaps.inaf.it (MF); costanzo.federico@iaps.inaf.it (CF); simone.deangelis@iaps.inaf.it (SDA)

1.1 Origin

Several mechanisms have been invoked to explain the formation of Ceres. According to Turrini, Magni & Coradini (2011), Ceres accreted *in situ* in the outer main belt, its accretion being fed by the growth of the forming Jupiter core. Alternatively, Ceres could have formed in the Kuiper Belt at an initial temperature <50 K and then migrated towards the inner Solar system to its current position (McKinnon 2008; De Sanctis et al. 2015), in order to justify the observation of ammonia-bearing compounds.

Mousis & Alibert (2005) suggest that Ceres could have merged, during accretion, with metre-sized icy planetesimals that had migrated inward from the outer Solar system. These planetesimals contained volatile components in the form of clathrates, hydrates and condensates. They also suggest that measurement of the D/H ratio of Ceres' ices could be a valuable observational test.

Zolotov (2009, 2014) describe Ceres as formed by planetesimals constituted by hydrated silicates, after all ^{26}Al had decayed.

1.2 Internal structure

In the past, several models tried to describe the internal structure of Ceres, arriving at different conclusions: Ceres might have a differentiated structure (McCord & Sotin 2005; Thomas et al. 2005; Castillo-Rogez & McCord 2010; Castillo-Rogez 2011; Neveu & Desch 2015; Neveu, Desch & Castillo-Rogez 2015), while for other

models the result is a porous undifferentiated interior; see for example Zolotov (2009). A large amount of water ice is inferred from its low mean density of 2160 ± 8 kg m^{-3} (Park et al. 2016). As water is supposed still to be present inside Ceres, it can be argued that the amount of residual ^{26}Al at the end of accretion was not high enough to remove all water from the object.

According to Thomas et al. (2005), the oblate spheroidal shape of Ceres suggests that the dwarf planet is in hydrostatic equilibrium, having a mass concentration in the core (i.e. it is differentiated), while large internal voids are unlikely due to the high pressure. Consequently, the internal structure is constituted by a rocky core and an icy mantle, covered with a thin surface regolith layer of ice–silicate mixture.

McCord & Sotin (2005) modelled various scenarios, based substantially on different values of ^{26}Al/^{27}Al ratio available at the end of Ceres' formation process. For a fast accretion time (2.4 Myr), water ice would be stable below tens of metres of silicate regolith, while it would be unstable at the surface and would sublimate (McCord & Sotin 2005; Formisano et al. 2016).

Castillo-Rogez & McCord (2010) studied Ceres' internal differentiation and long-term evolution for different accretion times from calcium–alluminum rich inclusion (CAI) formation, in the range 1–10 Myr ($t_{0\text{-CAIs}}$). Substantial differences arise on moving from formation times <5 Myr to times >5 Myr, due to the different amount of residual ^{26}Al available within the newly accreted Ceres. In the former case, the object has a hydrated silicate-rich interior at the end of accretion, due to hydrothermal activity driven by ^{26}Al decay. In the case of a longer formation time, hydration of silicates could occur in the post-accretion phase.

Alternative models describing an undifferentiated Ceres have also been proposed. According to Zolotov (2009), the object could be nearly homogeneous, as suggested by measurements of the flattening and J_2 parameter (Carry et al. 2008). In this case, there is a high internal porosity and a low water ice content in the mantle, while a rocky crust would be highly unstable. However, the scenario proposed by Zolotov (2009) is a chemical model and is not supported by geophysical computations and modelling. Non-hydrostatic effects deduced from the gravity–topography data of the DAWN mission have been interpreted as indicative of a less differentiated structure (Ermakov et al. 2016). However, Castillo-Rogez (2011) has pointed out that high porosity in a large object like Ceres would unavoidably lead to instability.

In the model of Neveu et al. (2015), several scenarios are proposed depending on the formation time (2, 3 or 5 Myr after CAIs) and on the content of anti-freezing compounds (e.g. ammonia). If the ammonia concentration is a few per cent with respect to the water concentration, no liquid layers are present today and the internal structure consists of a dry inner core, a hydrated outer core and an icy crust. A larger ammonia concentration would allow the existence of liquid layers below the icy crust at the present day. In some cases ($t_0 = 2$ Myr), core cracking and hydrothermal circulation can occur (Neveu et al. 2015). In our work, the role of core cracking and hydrothermal circulation is neglected, since it is not well constrained: in this sense, Ceres gravity data from future missions will help.

A somewhat different model has been proposed by Neveu & Desch (2015), in which Ceres, at the end of accretion, is constituted by a chondritic core and a 'muddy' mantle consisting of a mixture of water ice and rock grains, both micrometre-sized. Depending on the time of formation after CAIs (less or more than 4 Myr), the object could have retained enough ^{26}Al to experience high internal temperature and melting throughout the entire interior or only at depth, respectively. At the end of thermal evolution, the object could have retained an internal liquid water ocean. The subsequent freezing of part of the ocean causes an increase of volume and pressure and water/brines mass uplift and outflow at the surface, with consequent cryovolcanism (Neveu & Desch 2015).

In the previously described models, the internal structure of Ceres is such that the density of the crust is larger than the density of the underlying mantle, being in principle gravitationally unstable, as also pointed out by Shoji & Kurita (2014). Moreover, Shoji & Kurita (2014) explore the possibility of explaining the water-vapour emission of Ceres (Küppers et al. 2014) by compositional diapirism, which exposes fresh ice on the surface. Other objects in the Solar system are characterized by crustal instability, among which, for example, is Callisto. Callisto has a crust composed of a rock–ice mixture (Nagel, Breuer & Spohn 2004), but in this case the crucial point is that the surface temperature is not greater than the critical one for Rayleigh–Taylor instability (i.e. 150 K) (Rubin, Desch & Neveu 2014). This allows Callisto and the Kuiper Belt objects, with the same peculiar structure, to preserve their undifferentiated crust during their evolution (Rubin et al. 2014). In the case of Ceres, surface temperatures (Formisano et al. 2016) can overcome the critical temperature and Rayleigh–Taylor instability is potentially possible. However, a crucial role in the onset (or not) of such instability is played by the viscosity of the layers, as we will discuss in this article.

In this work, starting from a differentiated structure, we analyse how the thickness and composition of the primordial crust can affect its stability. We apply a parametrized convection method to study the internal thermal evolution of the object. We select two configurations: one is characterized by a dehydrated silicate core, a pure ice mantle and an undifferentiated crust, while the other is characterized by a hydrated silicate core, a muddy mantle and a primordial crust. Both configurations assume Ceres as a differentiated object, based on the indications provided by recent measurements of the mean moment of inertia (Park et al. 2016), which tend to exclude a higher porous internal structure. The choice of models characterized by a pure ice mantle or a muddy mantle is linked to the presence or otherwise of silicate impurities in the icy mantle, as we will discuss in Section 3. Since this ambiguity is present in the literature, we performed our simulations considering both configurations.

We structured the article in the following way. In Section 2 we describe the model we have used for our simulations, touching on the viscosity laws adopted, and in Section 3 we introduce the configurations we have studied, while in Sections 4 and 5 the results and discussion are reported, respectively.

2 THE MODEL

2.1 General equations

The numerical modelling developed here utilizes parametrized thermal convection: each layer that composes Ceres is characterized by a single temperature and for each of them the conservation of energy is imposed. In the literature, there are many works that adopt this scheme (Schubert 1979; Stevenson, Spohn & Schubert 1983; McNamara & van Keken 2000; Solomatov & Moresi 2000; Korenaga & Jordan 2002; Freeman 2006; Grindrod et al. 2008; Korenaga 2009; Sterenborg & Crowley 2013). The equation to solve for each layer is

$$V \rho c_{\rm p} \frac{{\rm d}T}{{\rm d}t} = F_{\rm in} A_{\rm bottom} - F_{\rm out} A_{\rm top} + Q(t) V, \quad (1)$$

Table 1. Radiogenic heating parameters used in this model, provided by McCord & Sotin (2005).

Element	Initial concentration (C_0) [ppb]	Specific heat production (H_0) [mW kg^{-1}]	Half-lives [Ga]
^{238}U	52.4	0.104	4.47
^{235}U	17.5	0.401	0.70
^{232}Th	130.0	0.020	14.0
^{40}K	430.6	0.062	1.25

where V is the volume of the layer, ρ the density, c_p the specific heat, T the average temperature, F the heat flux, A the area of the layer and Q the radiogenic heat production per unit volume. The radiogenic heat is provided by long-lived radionuclides, i.e. ^{235}U, ^{238}U, ^{232}Th and ^{40}K, and is given for Ceres by (McCord & Sotin 2005, see also Table 1)

$$Q(t) = \rho x_s \sum_{i=1}^{n} C_0 H_0 \exp(-\lambda_i t), \tag{2}$$

where ρ is the density of the layer, x_s the mass fraction of silicates, C_0 the initial concentration, H_0 the initial power of radiogenic decay per unit mass of radiogenic element and λ_i the decay constant.

The heat flux in equation (1) is given by

$$F = \frac{K\Delta T}{D} Nu, \tag{3}$$

where K is the thermal conductivity, ΔT the temperature drop over the boundary layer, D the thickness of the layer and Nu the Nusselt number. The Nusselt number is associated with the thermal boundary layer (δ) by the relationship

$$\delta = D/Nu \tag{4}$$

and also linked to the Rayleigh number (Ra) by numerical simulations as

$$Nu = a \left(\frac{Ra}{Ra_{cr}} \right)^{\beta}, \tag{5}$$

where a and β are set to 1 and 0.255, respectively (Desch et al. 2009), and Ra_{cr} is a critical value typically set at 1000.

The Rayleigh number can be written as

$$Ra = \frac{\alpha g \rho \Delta T D^3}{\kappa \eta}, \tag{6}$$

where α is the thermal expansion, g the acceleration due to gravity, κ the thermal diffusivity and η the dynamic viscosity.

2.2 Boundary conditions

For each layer (j), the heat flow across the boundaries is calculated as follows:

$$F_{j,\text{in}} = F_{j-1,\text{out}}, \tag{7}$$

where the flux that enters the core is assumed to be zero, while at the external surface we fix the temperature at 163 K, i.e. the temperature for a surface in radiative equilibrium at the Ceres mean orbital radius, by assuming a solar constant of 175 W m^{-2}.

2.3 Viscosity laws

For the 'rock', we use a viscosity law depending on the average temperature of the layer (Grindrod et al. 2008) and on the melting degree (Sterenborg & Crowley 2013):

$$\eta_{\text{rock}} = \eta_{0,\text{rock}} \exp\left[\frac{E}{R T_{\text{melt,rock}}} \left(\frac{T_{\text{melt,rock}}}{T} - 1 \right) \right] \exp(-C\chi), \tag{8}$$

where $\eta_{0,\text{rock}}$ is the viscosity of the rock at the zero-pressure melting point, $T_{\text{melt,rock}}$ the melting temperature of the rock, E the activation energy, R the gas constant and χ the melting degree. The melting constant C is set to be 25, which corresponds to the case of diffusive creep (Reese & Solomatov 2006).

For the water ice viscosity, we use the Arrhenius law as in Shoji & Kurita (2014):

$$\eta_{\text{ice}} = \eta_{0,\text{ice}} \exp\left[B \left(\frac{T_{\text{melt,ice}}}{T} - 1 \right) \right], \tag{9}$$

where B is set to 25 (Desch et al. 2009), $\eta_{0,\text{ice}}$ is the reference viscosity for water ice and $T_{\text{melt,ice}}$ the melting temperature of the water ice.

How to calculate the viscosity of a mixture of ice–rock is matter of debate in the literature. Shoji & Kurita (2014) modify the ice viscosity by dividing it using a weight-function of the volumetric percentage of silicate in the icy matrix:

$$\eta_{\text{mix}} = \frac{\eta_{\text{ice}}}{f(\phi)}, \tag{10}$$

where $f(\phi)$ takes into account the volume fraction of the rock in the mixture as (Shoji & Kurita 2014)

$$f(\phi) = \left(1 - \frac{\phi}{\phi_{\text{CPL}}} \right)^{\gamma}, \tag{11}$$

where γ is a constant fixed at 2.0 (Shoji & Kurita 2014), ϕ the volume fraction of the rock and ϕ_{CPL} the rock fraction at the close-packing limit, set at 0.74. Another method is provided by Friedson & Stevenson (1983), which uses the following relationship (also used in Freeman 2006) for the viscosity of the mixture:

$$\eta_{\text{mix}} = \eta_r(\phi)\, \eta_0 \exp\left[25 \left(\frac{T_{\text{melt,ice}}}{T} - 1 \right) \right], \tag{12}$$

where $\eta_r(\phi)$ is the relative viscosity given by the empirical formula

$$\eta_r = 1 + 2.5\phi + 10.05\phi^2 + 0.00273 \exp(16.6\phi). \tag{13}$$

This assumption is valid for $0 \leq \phi \leq 0.6$ (see also fig. 3 of Mangold et al. 2002). In our case, ϕ ranges from 0.7–0.9; for this reason we have decided to use the following approximation:

$$\eta_{\text{mix}} = \eta_{\text{sil}}^{\phi} \eta_{\text{ice}}^{(1-\phi)}, \tag{14}$$

which is a log average between ice and rock viscosity weighted by the fraction of rock. This relationship permits us to recover the limits of pure ice and pure rock.

In order to study the stability of the crust, we have to define a critical viscosity as in Rubin et al. (2014) and in Shoji & Kurita (2014):

$$\eta_{\text{crit}} = \left[(n-1)^{1/n} \frac{C_{L\Delta\rho}}{2n} \right] \left(\frac{Z_0}{L} \right)^{(n-1)/n} \Delta\rho g L t, \tag{15}$$

where n is the index of the stress σ related to the strain rate: we set this index at 1.8, as in Shoji & Kurita (2014). $C_{L\Delta\rho}$ is a dimensionless quantity depending on the geometry and rheology and its value is

Table 2. Physical parameters used in our simulations.

	Value	Units	Ref.
General parameters			
Radius	470	km	—
Mass	9.395×10^{20}	kg	Thomas et al. (2005)
Density	2162.5	kg m^{-3}	Park et al. (2016)
Surface temperature	163	K	—
Surface gravity	0.29	m s^{-1}	—
Gravitational constant	6.67×10^{-11}	m^3 kg^{-1} s^{-2}	—
Gas constant	8.3144	J mol^{-1} K^{-1}	—
Stefan–Boltzmann constant	5.67×10^{-8}	W m^{-2} K^{-4}	—
Silicate parameters			
Density (dehydrated)	3250	kg m^{-3}	Rubin et al. (2014)
Density (hydrated)	2900	kg m^{-3}	Neveu & Desch (2015)
Specific heat	$\begin{cases} 770\,(T/275) & \text{for} 0 \le T < 275K \\ 607 + 163\,(T/275) & \text{for} 275 \le T < 1000K \\ 1200 & \text{for} T > 1000\,K \end{cases}$	J kg^{-1} K^{-1}	Desch et al. (2009)
Thermal conductivity (dehydrated)	4.2	W m^{-1} K^{-1}	Ellsworth & Schubert (1983)
Thermal conductivity (hydrated)	1.0	W m^{-1} K^{-1}	Neveu et al. (2015)
Thermal expansivity	3×10^{-5}	K^{-1}	Ellsworth & Schubert (1983)
Activation energy	525	kJ mol^{-1}	McNamara & van Keken (2000)
Reference viscosity	10^{21}	Pa s	McNamara & van Keken (2000)
Solidus temperature	1425	K	Sterenborg & Crowley (2013)
Liquidus temperature	1800	K	Sterenborg & Crowley (2013)
Ice parameters			
Density	950	kg m^{-3}	Grindrod et al. (2008)
Specific heat	7.037T + 185.0	J kg^{-1} K^{-1}	Ellsworth & Schubert (1983)
Thermal conductivity	$4.88 \times 10^2/T + 0.467$	W m^{-1} K^{-1}	Ellsworth & Schubert (1983)
Thermal expansivity	$2.5 \times 10^{-7}T - 1.25 \times 10^{-5}$	K^{-1}	Ellsworth & Schubert (1983)
Activation energy	60	kJ mol^{-1}	Durham & Stern (2001); Grindrod et al. (2007)
Reference viscosity	10^{14}	Pa s	Shoji & Kurita (2014)
Melting temperature	273.0	K	—

about 0.76 (Molnar, Houseman & Conrad 1998; Rubin, Desch & Neveu 2014; Shoji & Kurita 2014): this value is valid in the limit $L/h \rightarrow 0$ (Molnar et al. 1998), where h represents the thickness of the crust. $\Delta\rho$ is the contrast in density between the crust and the mantle. Z_0 is the initial perturbation amplitude (in this work we set it at 0.01 L), with L provided by (Shoji & Kurita 2014)

$$L = \frac{nRT_0}{E_a}\frac{T_0}{|\,\mathrm{d}T/\mathrm{d}z\,|}, \tag{16}$$

where T_0 is the temperature at the interface between crust and icy mantle, E_a is the activation energy, set at 49 kJ mol^{-1} (Shoji & Kurita 2014), and $\mathrm{d}T/\mathrm{d}z$ is the temperature gradient across the crust. L is the length-scale over which the maximum change in viscosity occurs. In our simulations, we use $L/h \le 0.4$, as inferred from fig. 9 of Molnar et al. (1998). The wavelength (λ) of the perturbation is of the order of L, as discussed in Rubin et al. (2014); moreover, λ is very small with respect to the radius of the asteroid and this allows us to neglect curvature effects in the Rayleigh–Taylor instability analysis.

All the physical parameters used in this work are reported in Table 2.

3 CERES STRUCTURES AND INITIAL TEMPERATURE

We have explored two main different configurations: in the first, case A, we consider a differentiated structure composed of a dehydrated silicate core (370 km), a pure ice mantle (about 100 km) and a crust made of a mixture of ice and silicate (ranging from 1–10 km); in case B, we consider a hydrated silicate core of 370 km, a 'muddy' mantle (ice with silicate impurities) of about 100 km and a crust similar to the previous case. In Fig. 1, the scheme of the internal structures we analysed is reported. In both cases, we considered that the crust remains undifferentiated and no metals are present in the core: this could be true given the low mean density, even if in the literature this possibility is contemplated (McCord & Sotin 2005). In both cases, again, the density of the crust is equal to 3020, 2790and 2560 kg m^{-3} for ice contents of 10, 20 and 30 per cent by volume, respectively: we observe that the crust is always more dense than the mantle.

The possibility of having a pure ice mantle is a matter of debate in the literature, as discussed by Neveu & Desch (2015). Several works assumed a pure ice mantle (McCord & Sotin 2005; Castillo-Rogez & McCord 2010; Neveu et al. 2015). In contrast, there are some motivations against the idea of a pure ice mantle. The surface of Ceres is mainly constituted by aqueously altered minerals (phyllosilicates) rather than ice (De Sanctis et al. 2015); a mantle of ice with silicate impurities is required if we accept the idea that, for example, an endogenous process put hydrated minerals on Ceres' surface, interpreted as a lag deposit. The ice inside the crater easily sublimates down to a depth of a few metres (equatorial and midlatitudes: Fanale & Salvail 1989). We refer the reader to Neveu & Desch (2015) for a more complete discussion of the problem.

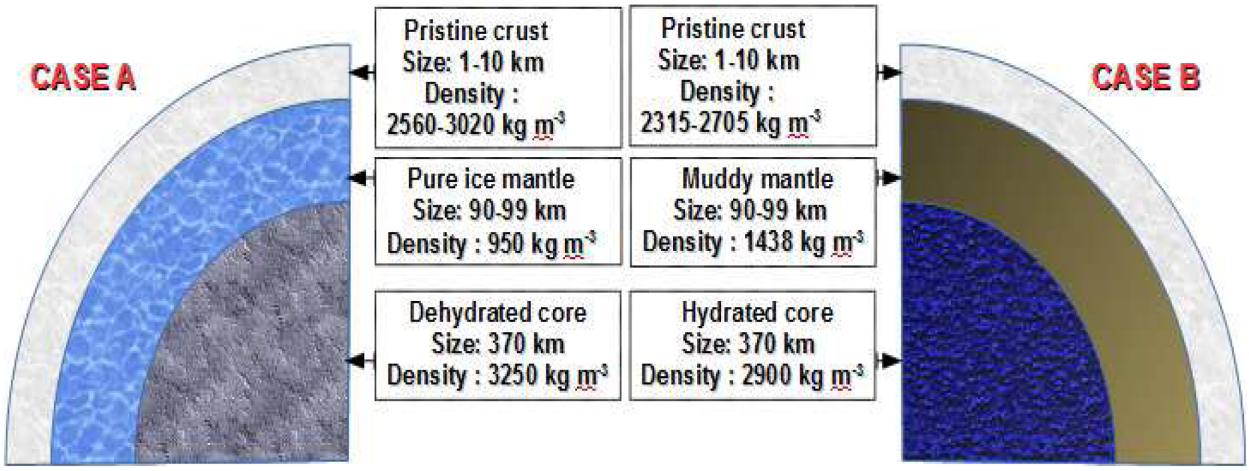

Figure 1. Internal structures of Ceres considered in this work: on the left (case A) a structure with a dehydrated core and a pure ice mantle and on the right (case B) a structure with a hydrated core and a muddy mantle (ice with silicate impurities). The figure is not to scale.

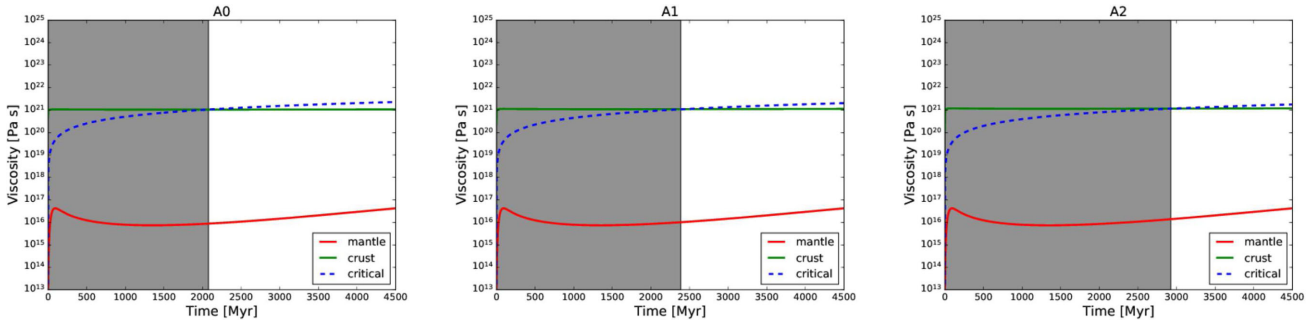

Figure 2. Icy mantle (case A): viscosity plot in the case of crust thickness 1 km and (a) 10, (b) 20 and (c) 30 per cent by volume of ice in the crust. The grey box indicates the crust stability timespan, defined as the intersection between the viscosity of the crust and the critical value.

The initial temperatures considered in our simulations are compatible with modelling results present in the literature (e.g. McCord & Sotin 2005; Neveu & Desch 2015): we start with a core temperature of 500 K, a mantle at 300 K and a crust at 200 K, which exchanges heat with the environment at 163 K. The starting point is a post-differentiated structure, in which short-lived radionuclides have decayed and only long-lived ones are operating.

4 RESULTS

4.1 Crust stability

We begin by discussing the results of case A, in which the mantle is made of pure ice, with a density of 950 kg m^{-3} and a core that is not hydrated, with a density of 3250 kg m^{-3} typical of ordinary chondrites (Rubin et al. 2014). In Fig. 2 (crust of 1 km), the plot of viscosity (for mantle and crust, plus the critical viscosity) versus time up to 4.5 Gyr is shown. In this figure, as in the subsequent ones, we do not report the core viscosity, since it is always constant. The core viscosity is constant because the temperature does not become higher than the melting point of the silicate, while the mantle viscosity exhibits a trend compatible with the behaviour of the temperature, as we will see in the following. As discussed by Rubin et al. (2014), if the viscosity of the crust is less than the critical viscosity, calculated according to equation (15), the Rayleigh–Taylor instability can operate while, if the viscosity of the crust becomes greater than its critical value, the crust is stable. From Fig. 2 we deduce that models A0–A2 have a crust that is stable for a timespan between 2 and 3 Gyr. The stability time can be deduced by the intersection between the viscosity of the crust and the critical value, so the grey box individuates the stability timespan. If we increase the thickness of the crust, we observe a general decrease in crust stability, as revealed in Figs 3 and 4. In Fig. 3, the case of a crust of 5 km is shown: if the ice in the crust is 10 per cent by volume, the stability is only a few thousands of years, the primordial crust is 'immediately' lost and the stability timespan is less than 500 Myr. The new crust could be originated by chemical mixing between the unstable primordial crust and the ice mantle. If we increase the percentage of ice in the crust, the stability increases slightly up to about 500 Myr (model A5). Finally, we consider a crust of 10 km (Fig. 4). Model A6 has a crust that is 'always' unstable, since the viscosity of the crust never becomes greater than the critical value, as in A7 and A8, for which the trend and the time-scales are essentially the same. In this latter case (10 km), the thickness of the crust is large enough not to allow the survival of the primordial crust. In Table 3, the main physical characteristics of the models studied are summarized, including the errors in the density, having assumed 2162±8 kg m^{-3} as a reference value of the mean density (Park et al. 2016). The mean moment of inertia of Ceres for the different structures considered has also been computed. The most reasonable model, according to the value of the mean density is A8. In fact, this model has an error in the density equal to 0.5 per cent and is also characterized by a moment of inertia of 0.333. We recall

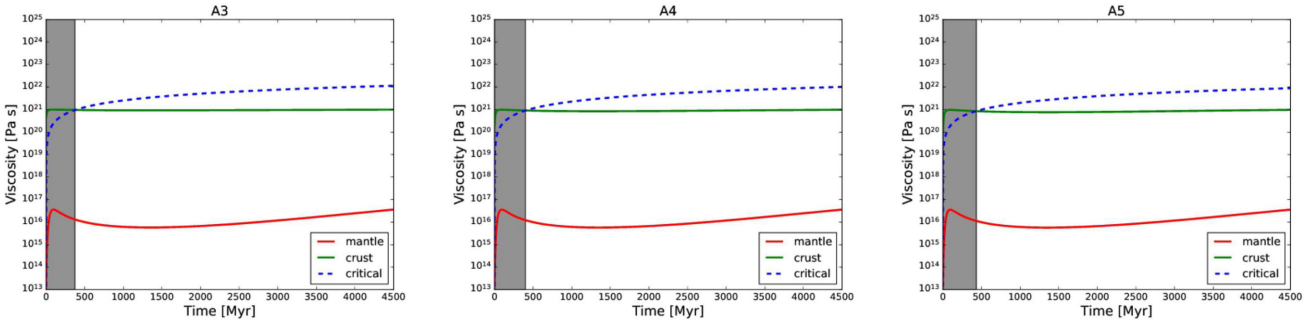

Figure 3. Icy mantle (case A): viscosity plot in the case of crust thickness 5 km and (a) 10, (b) 20 and (c) 30 per cent by volume of ice in the crust. The grey box indicates the crust stability timespan, defined as the intersection between the viscosity of the crust and the critical value.

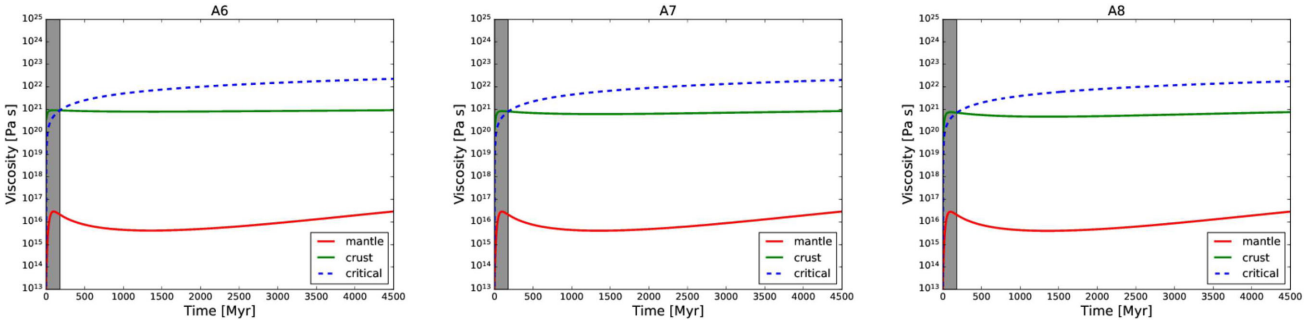

Figure 4. Icy mantle (case A): viscosity plot in the case of crust thickness 10 km and (a) 10, (b) 20 and (c) 30 per cent by volume of ice in the crust. The grey box indicates the crust stability timespan, defined as the intersection between the viscosity of the crust and the critical value.

Table 3. Summary of the models developed, in the case of a pure ice mantle (case A). From left to right: the model, the crust thickness in km, the percentage of ice (by volume) in the crust, the mean density of the structure (in kg m^{-3}), the error in the density (assuming the measured value of 2162 kg m^{-3}) and the dimensionless moment of inertia. The model with the lowest error in the mean density is A8.

Model	Crust thickness [km]	Ice vol. per cent	$\rho_{\mathrm{mean,\,calc}}$ [kg m^{-3}]	Err_ρ(per cent)	MoI
A0	1	10	2085	3.6	0.320
A1	1	20	2084	3.6	0.320
A2	1	30	2082	3.7	0.319
A3	5	10	2137	1.1	0.330
A4	5	20	2130	1.5	0.327
A5	5	30	2123	1.9	0.326
A6	10	10	2201	1.8	0.337
A7	10	20	2187	1.1	0.335
A8	10	30	2172	0.5	0.333

that the value of 0.4 corresponds to a homogeneous sphere, while values less than 0.4 result in a differentiated structure, with the inner layer denser than the outer ones. In the literature, there are some estimations of the moment of inertia of Ceres: for example, Rambaux et al. (2011), with a three-layer model, estimated a value of 0.347 by using the rotational momentum of Ceres. A more recent work (Park et al. 2016), using a two-layer model (a core of about 280 km and an outer shell of about 190 km), has inferred a value of the moment of inertia of 0.36. Finally, in Rambaux, Chambat & Castillo-Rogez (2015) the mean moment of inertia ranges from 0.347 to 0.356 for two-layer and four-layer models, respectively.

In case B, we have analysed a structure of Ceres comprising a hydrated core, with a density of 2900 kg m^{-3}, and a 'muddy' mantle, i.e. an icy mantle with silicate impurities, the density of which is about 1440 kg m^{-3}: also, in this case, the crust is a mixture of ice and silicates in different ratios. The general trend that we observe in Figs 5, 6 and 7 is an increase in the stability time of the crust, due to the higher density of the underlying mantle with respect to the previous case A. In Fig. 5, the crust has a thickness of 1 km and its stability time is very long: in the case of 10 per cent by volume of ice (B0), it is around 3 Gyr, while in the other two cases (20 and 30 per cent by volume of ice) the crust is stable for about 3.5 Gyr (B1) and for the whole lifetime of the Solar system (B2), respectively. In this last case, what we currently observe could be the primordial crust. The model with 5 km has a stable crust for about 500 Myr (B3 and B4) and about 700 Myr (B5), as we can see in Fig. 6. The last case (see Fig. 7) is generally unstable, with a value of stability timespan around 250 Myr. Like the previous case, in Table 4 a summary of the models is reported: the model with the lowest error in the density, hence more likely, turns out to be B2, with an error of about 0.2 per cent and a mean moment of inertia of 0.351.

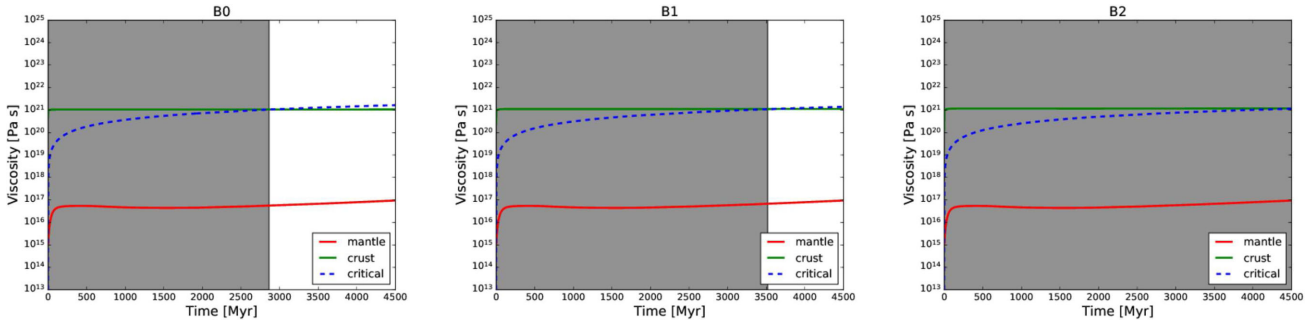

Figure 5. Muddy mantle (case B): viscosity plot in the case of crust thickness 1 km and (a) 10, (b) 20 and (c) 30 per cent by volume of ice in the crust. The grey box indicates the crust stability timespan, defined as the intersection between the viscosity of the crust and the critical value.

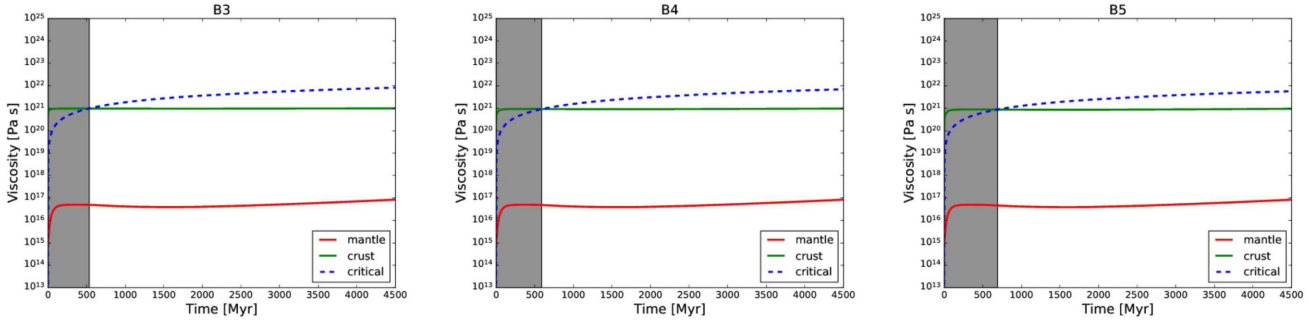

Figure 6. Muddy mantle (case B): viscosity plot in the case of crust thickness 5 km and (a) 10, (b) 20 and (c) 30 per cent by volume of ice in the crust. The grey box indicates the crust stability timespan, defined as the intersection between the viscosity of the crust and the critical value.

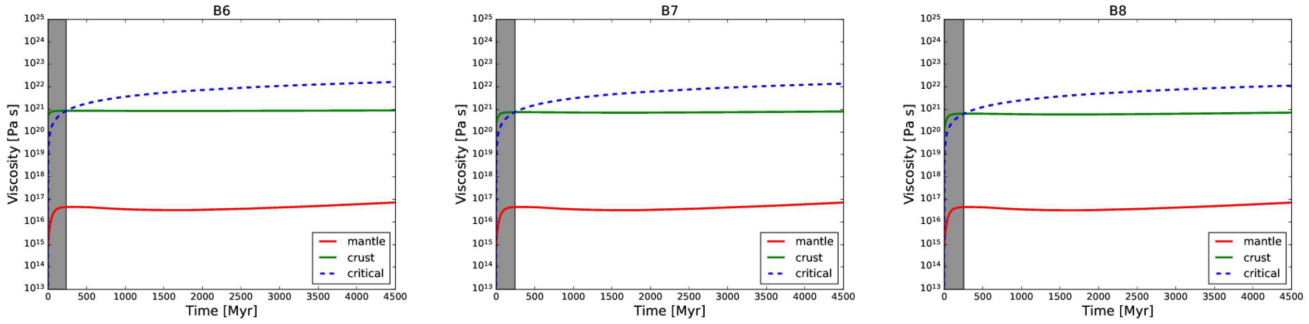

Figure 7. Muddy mantle (case B): viscosity plot in the case of crust thickness 10 km and (a) 10, (b) 20 and (c) 30 per cent by volume of ice in the crust. The grey box indicates the crust stability timespan, defined as the intersection between the viscosity of the crust and the critical value.

Table 4. Summary of the models developed, in the case of a 'muddy' ice mantle (case B). From left to right: the model, the crust thickness in km, the percentage of ice (by volume) in the crust, the mean density of the structure (in kg m^{-3}), the error in the density (assuming the measured value of 2162 kg m^{-3}) and the dimensionless moment of inertia. The model with the lowest error in the mean density is B2.

Model	Crust thickness [km]	Ice vol. per cent	$\rho_{\text{mean, calc}}$ [kg m^{-3}]	Err_ρ(per cent)	MoI
B0	1	10	2205	1.9	0.355
B1	1	20	2203	1.9	0.355
B2	1	30	2158	0.2	0.351
B3	5	10	2243	3.7	0.360
B4	5	20	2236	3.4	0.359
B5	5	30	2229	3.1	0.358
B6	10	10	2289	5.9	0.366
B7	10	20	2274	5.2	0.364
B8	10	30	2261	4.5	0.362

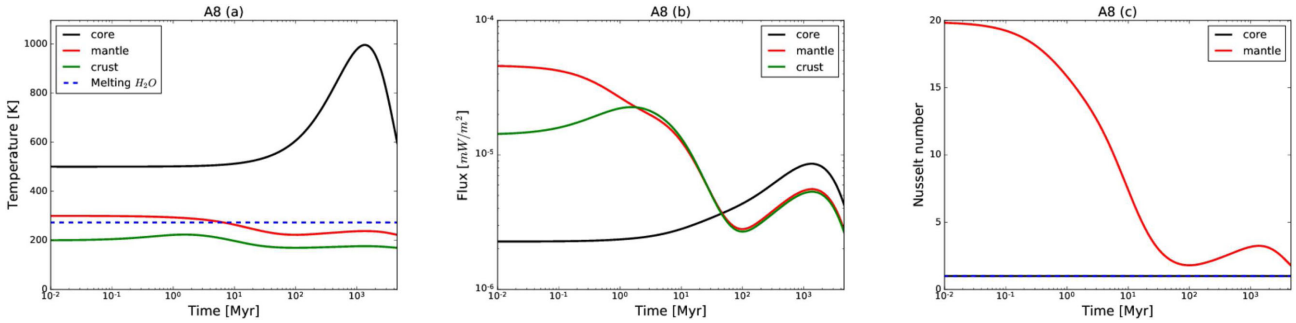

Figure 8. Model A8: (a) temperature and (b) output heat flux for the different layers and (c) a Nusselt number versus time plot for the core and mantle. If the Nusselt number is greater than unity (dotted line in panel (c)), thermal convection is possible.

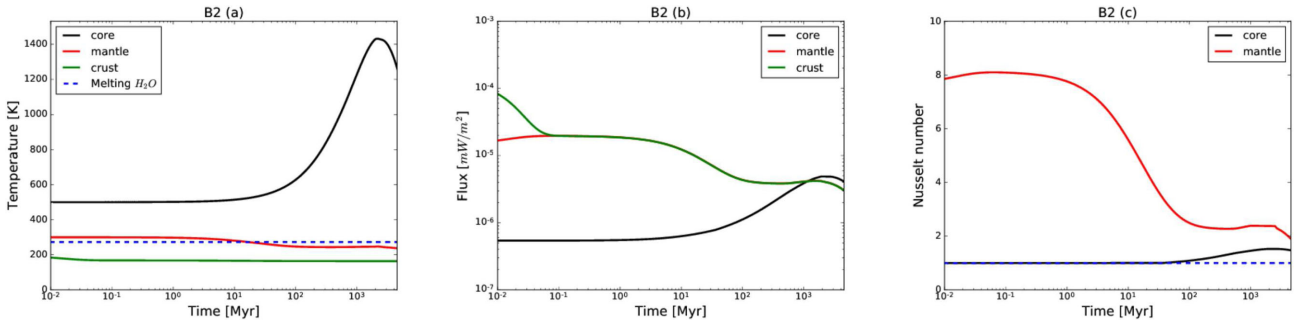

Figure 9. Model B2: (a) temperature and (b) output heat flux for the different layers and (c) a Nusselt number versus time plot for the core and mantle. If the Nusselt number is greater than unity (dotted line in panel (c)), thermal convection is possible.

4.2 Temperature, flux and Nusselt number profiles

For the two plausible models in both A and B cases, i.e. A8 and B2, we report in Figs 8 and 9 the behaviour of the temperature and output heat flux of the different layers and the Nusselt number of the core and mantle, respectively. We recall that the Nusselt number quantifies how strong the heat convection is with respect to the heat conduction. In Fig. 8(a), we observe that the maximum temperature reached in the core, in the case of a pure ice mantle, is around 900 K after 1 Gyr. The scale used on the x-axis is logarithmic in order to highlight the general trend at the beginning of the simulation. After 4.5 Gyr, i.e. today, the temperature of the core is about 600 K. We recall that no radiation boundary conditions are imposed, but the surface temperature is considered constant. In Fig. 8(a), the blue dashed line represents the melting point of the ice: we can see that the mantle has a temperature greater than 273 K before 10 Myr since the differentiation. In the literature, some theoretical models allow liquid water, buried in the interior layers, for about 100 Myr from the accretion (McCord & Sotin 2005; Castillo-Rogez 2011; Neveu & Desch 2015). Monotone trend in the sense of almost constant trend, except at the time of peak temperature of the core, where it tends to increase. The crust temperature is almost constant, around 200 K. The heat flux of the mantle (Fig. 8b) is dominant until 1 Myr, while after 20 Myr the heat flux emerging from the core becomes higher. In Fig. 8(c), the Nusselt number for the core and the mantle is reported. Concerning the mantle, it reaches high values (about 20), higher than the critical value (1, blue dashed line in the figure), for the onset of convection. The core Nusselt number is around 1.

Regarding case B2, we observe that the general trend is the same for temperature, while the peak in the core temperature is higher with respect to the previous case, about 1400 K after 1 Gyr (see Fig. 9a). This increase in temperature is due to the lower thermal conductivity in the case of a hydrated silicate core with respect to the case of dehydrated silicate and hence less efficiency in heat transmission towards the outer layers. The current core temperature is around 1200 K. Also, in this case, the 'water ocean' (it is probably more appropriate to define it as a 'muddy ocean') lasts for about 10 Myr. In Fig. 9(b), the heat fluxes from the mantle and the crust converge after 0.1 Myr and the core heat flux becomes predominant after 1 Gyr from the differentiation. The trend of the Nusselt number of the mantle is similar to the previous case, but the maximum value reached is now around 8. The Nusselt number of the core overcomes the critical value only after $\simeq$100 Myr from differentiation. During the entire time of the simulation, the Nusselt numbers of the core and mantle are higher than the critical value (Fig. 9c).

5 DISCUSSION AND CONCLUSIONS

In this article, we have explored the physical conditions for stability of the crust of the dwarf planet Ceres, considering a post-differentiation structure in which the heating contribution is provided only by long-lived radionuclides.

We performed several simulations varying the composition of the crust and its thickness, using two main configurations: case A with a dehydrated core and a pure ice mantle and case B with a hydrated core and a muddy mantle. The crust, in both cases, is made of a mixture of ice and rock in well-defined proportions. The peculiarity of the crust is that it is gravitationally unstable, being denser than the underlying mantle and so subject to Rayleigh–Taylor instability. Rubin et al. (2014) found that crust overturn is possible if the crust has a temperature greater than 150 K: this conclusion, in general, seems to be in agreement with our results.

Our simulations also suggest that, in the case of a pure ice mantle, the crust is always unstable. In the case of a crust thickness of 1 km and low ice volumetric percentage, the stability time is about 3 Gyr, while in the cases of 5 and 10 km crust thickness the stability time is less than 500 Myr. Conversely, in the case of a muddy mantle, the crust is stable until the present if it is 1 km deep and has 30 per cent by volume of ice, while in the other cases (5–10 km) the stability time is always less than 1 Gyr. It should be noted that the Rayleigh–Taylor instability could operate only in particular unstable regions of the surface and not on the entire surface. This means that the crust could exhibit anisotropies in density. The gravitational energy associated with overturn of the crust could trigger localized water emission. *Herschel* observations (Küppers et al. 2014) have suggested a water flux emission of about 6 kg s^{-1}, which corresponds to an emitting area less than 1 km^2 from pure ice exposure. Our results seem to indicate that the unstable wavelength is of the order of 0.4*L*, implying a thickness of the crust less than 3 km in order to justify the dimensions of the emitting area. This suggestion needs to be investigated further. On the other hand, the putative dependence of *Herschel* measurements on heliocentric distance would point towards the hypothesis of cometary-type emission (Küppers et al. 2014). In order to test this mechanism, in Formisano et al. (2016) we performed numerical simulations, which suggested that the ice on the surface is very unstable. The same result was obtained by Titus (2015). Moreover, the water flux proposed by *Herschel* can be matched if the sublimation comes from ice buried a few centimetres below the surface (compatible with the annual skin depth) (Formisano et al. 2016).

In the current work, we find that a water ocean (pure or muddy) lasts for about 10 Myr after differentiation. The possibility of a water ocean for about 100 Myr after accretion is already contemplated in the literature (McCord & Sotin 2005; Castillo-Rogez 2011; Neveu & Desch 2015). The temperatures obtained in our modelling rule out the idea that at present liquid water is buried in the interior of Ceres, even if in McCord & Sotin (2005) it is suggested that liquid water may be present today in the interior of Ceres. The occurrence of NH_4 phyllosilicates on Ceres' surface (De Sanctis et al. 2015) could be a clue to the subsurface presence of antifreezing compounds (ammonia) that would justify the presence of liquid water in the interior today, as also suggested by De Sanctis et al. (2016).

Based on the latest results obtained by the *Dawn* gravity measurements (Park et al. 2016), we propose two differentiated structures, one for case A and one for case B, as more likely:

(i) model A8, with a dehydrated core of 370 km, a pure ice mantle of 90 km and a crust of 10 km with 30 per cent by volume of ice, with a mean moment of inertia of 0.333;

(ii) model B2, with a hydrated core of 370 km, a muddy mantle of 99 km and a crust of 1 km with 10 per cent by volume of ice, with a mean moment of inertia of 0.351.

Future *Dawn* observations and gravity measurements will surely provide more correct answers regarding the complex internal structure of Ceres.

ACKNOWLEDGEMENTS

We are greatly indebted to Dr J. Roberts for his very useful comments and suggestions, which largely improved our work. This work is supported by an AGENZIA SPAZIALE ITALIANA (ASI) grant.

REFERENCES

Carry B., Dumas C., Fulchignoni M., Merline W. J., Berthier J., Hestroffer D., Fusco T., Tamblyn P., 2008, A&A, 478, 235
Castillo-Rogez J. C., 2011, Icarus, 215, 599
Castillo-Rogez J. C., McCord T. B., 2010, Icarus, 205, 443
De Sanctis M. C. et al., 2012, Science, 336, 697
De Sanctis M. C. et al., 2015, Nature, 528, 241
De Sanctis M. C. et al., 2016, Nature, 536, 54
Desch S. J., Cook J. C., Doggett T. C., Porter S. B., 2009, Icarus, 202, 694
Durham W. B., Stern L. A., 2001, Ann. Rev. Earth Planet. Sci., 29, 295
Ellsworth K., Schubert G., 1983, Icarus, 54, 490
Ermakov A. E., Zuber M. T., Smith D. E., Fu R. R., Raymond C. A., Park R. S., Russell C. T., 2016, in 47th Lunar and Planetary Science Conference, LPI Contribution No. 1903, p. 1708
Fanale F. P., Salvail J. R., 1989, Icarus, 82, 97
Formisano M., De Sanctis M. C., Magni G., Federico C., Capria M. T., 2016, MNRAS, 455, 1892
Freeman J., 2006, Planet. Space Sci., 54, 2
Friedson A., Stevenson D., 1983, Icarus, 56, 1
Grindrod P. M., Fortes A. D., Nimmo F., Feltham D. L., Brodholt J. P., Vočadlo L., 2008, Icarus, 197, 137
Korenaga J., 2009, Geophys. J. Int., 179, 154
Korenaga J., Jordan T. H., 2002, Geophys. Res. Lett., 29, 29, 1923
Küppers M. et al., 2014, Nat, 505, 525
Mangold N., Allemand P., Duval P., Geraud Y., Thomas P., 2002, Planet. Space Sci., 50, 385
McCord T. B., Sotin C., 2005, J. Geophys. Res. (Planets), 110, 5009
McKinnon W. B., 2008, in BAAS, AAS/Division for Planetary Sciences Meeting Abstracts #40, p. 464
McNamara A. K., van Keken P. E., 2000, Geochemistry, Geophysics, Geosystems, 1, 1027, 1027
McSween H. Y. et al., 2013, Meteoritics and Planetary Science, 48, 2090
Milani A., Cellino A., Knežević Z., Novaković B., Spoto F., Paolicchi P., 2014, Icarus, 239, 46
Molnar P., Houseman G. A., Conrad C. P., 1998, Geophys. J. Int., 133, 568
Mousis O., Alibert Y., 2005, MNRAS, 358, 188
Nagel K., Breuer D., Spohn T., 2004, Icarus, 169, 402
Neveu M., Desch S. J., 2015, Geophys. Res. Lett, 42, 10197
Neveu M., Desch S. J., Castillo-Rogez J. C., 2015, J. Geophys. Res. (Planets), 120, 123
Park R. S. et al., 2016, in 47th Lunar and Planetary Science Conference, LPI Contribution No. 1903, p. 1781
Rambaux N., Castillo-Rogez J., Dehant V., Kuchynka P., 2011, A&A, 535, A43
Rambaux N., Chambat F., Castillo-Rogez J. C., 2015, A&A, 584, A127
Reese C., Solomatov V., 2006, Icarus, 184, 102
Rivkin A. S., Asphaug E., Bottke W. F., 2014, Icarus, 243, 429
Rubin M. E., Desch S. J., Neveu M., 2014, Icarus, 236, 122
Russell C. T., Raymond C. A., 2011, Space Sci. Rev., 163, 3
Schubert G., 1979, Ann. Rev. Earth Planet. Sci., 7, 289
Shoji D., Kurita K., 2014, J. Geophys. Res. (Planets), 119, 2457
Solomatov V. S., Moresi L.-N., 2000, J. Geophys. Res. (Planets), 105, 21795
Sterenborg G., Crowley J. W., 2013, Phys. Earth Planetary Interiors, 214, 53
Stevenson D. J., Spohn T., Schubert G., 1983, Icarus, 54, 466
Thomas P. C., Parker J. W., McFadden L. A., Russell C. T., Stern S. A., Sykes M. V., Young E. F., 2005, Nat, 437, 224
Titus T. N., 2015, J. Geophys. Res. (Planets), 42, 2130
Turrini D., Magni G., Coradini A., 2011, MNRAS, 413, 2439
Zolotov M. Y., 2009, Icarus, 204, 183
Zolotov M. Y., 2014, Icarus, 228, 13

This paper has been typeset from a TEX/LATEX file prepared by the author.